ACS NANO

www.acsnano.org

Reconfiguring Organic Color Centers on the sp^2 Carbon Lattice of Single-Walled Carbon Nanotubes

Haoran Qu, Xiaojian Wu, Jacob Fortner, Mijin Kim, Peng Wang, and YuHuang Wang*

Cite This: *ACS Nano* 2022, 16, 2077−2087

Read Online

ACCESS | Metrics & More | Article Recommendations | Supporting Information

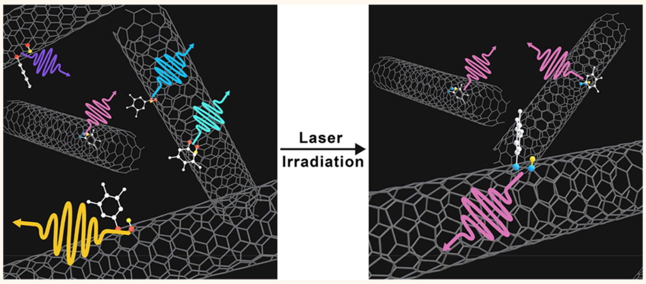

ABSTRACT: **Organic color centers (OCCs) are atomic defects that can be synthetically created in single-walled carbon nanotube hosts to enable the emission of shortwave infrared single photons at room temperature. However, all known chemistries developed thus far to generate these quantum defects produce a variety of bonding configurations, posing a formidable challenge to the synthesis of identical, uniformly emitting color centers. Herein, we show that laser irradiation of the nanotube host can locally reconfigure the chemical bonding of aryl OCCs on (6,5) nanotubes to significantly reduce their spectral inhomogeneity. After irradiation the defect emission narrows in distribution by ∼26% to yield a single photoluminescence peak. We use hyperspectral photoluminescence imaging to follow this structural transformation on the single nanotube level. Density functional theory calculations corroborate our experimental observations, suggesting that the OCCs convert from kinetic structures to the more thermodynamically stable configuration. This approach may enable localized tuning and creation of identical OCCs for emerging applications in bioimaging, molecular sensing, and quantum information sciences.**

KEYWORDS: *single-walled carbon nanotube, single-defect spectroscopy, atomic structure, photoluminescence, quantum defects*

Organic color centers (OCCs) are quantum defects that can be synthetically incorporated into single-walled carbon nanotube (SWCNT) hosts by covalently attaching organic functional groups to the sp^2 carbon lattice.[1−5] These sp^3 defects are exciton traps that produce bright photoluminescence (PL) in the shortwave infrared. The defect emission, labeled as E_{11}^-, is distinctly different and red-shifted from the E_{11} exciton PL native of the nanotube host.[4,6] Notably, the energy of E_{11}^- can be molecularly tuned in the near-infrared range by changing either the OCC functional group or nanotube chirality.[4,7] Furthermore, some OCCs have been shown to generate single photons at room temperature with a high purity of 99% along with excellent photostability.[8,9] Additionally, these single photons can occur in the telecom O-band with high indistinguishability,[10] making OCCs promising candidates for solid-state quantum technologies.[11] However, all known chemistries used to generate OCCs produce a variety of bonding configurations that result in a broad distribution of multiple emission peaks,[1,3−6,12−15] which pose a significant materials and synthetic challenge to solid-state quantum technologies.

The diverse atomic configurations of OCCs arise from addition reactions to the double bonds of the graphitic host, which can produce a pair of functional groups for every OCC in various possible bonding configurations. For example, diazonium chemistry, the most widely used approach for generating OCCs,[4,6,15,16] is believed to leave a reactive carbon at either the adjacent (ortho) positions or three carbons away (para) from the first bonding carbon.[17] These reactive species then presumably bond to an available H or OH group to complete the reaction.[17,18] This pair of functional groups may take one of many possible positions on the sp^2 carbon lattice, resulting in a large number of bonding configurations that are chemically, thermodynamically, and energetically distinct.[12,18,19] As a result, multiple OCC emission peaks are observed when carbon nanotubes, such as (6,5)-SWCNTs, are

Received: September 1, 2021
Accepted: January 13, 2022
Published: January 18, 2022

https://doi.org/10.1021/acsnano.1c07669
ACS Nano 2022, 16, 2077−2087

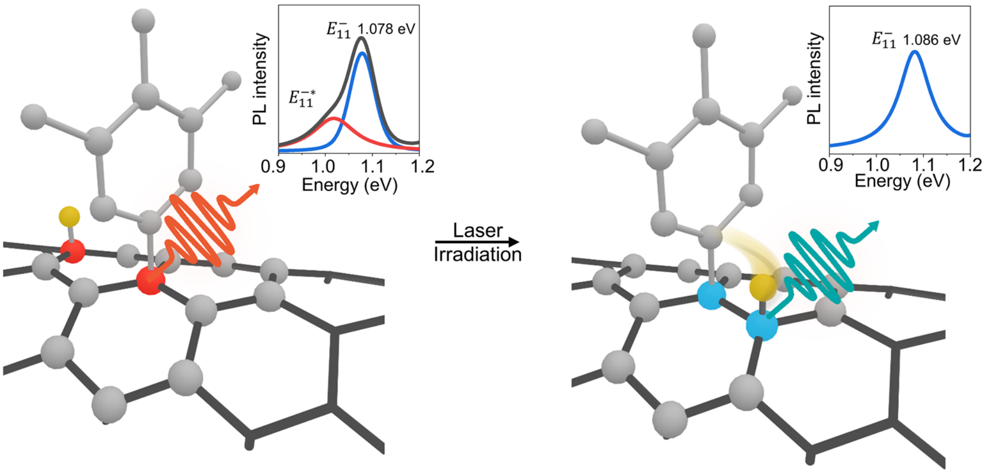

Figure 1. Laser irradiation transforms kinetic bonding configurations of OCCs to the thermodynamically stable structure on the sp^2 carbon lattice of semiconducting carbon nanotubes. The schematic shows an OCC that consists of an aryl group along with a pairing −H group (yellow atom) covalently attached to the sidewall of a (6,5)-SWCNT. The pairing −H group can attach to carbon at different locations (an example of the para configuration is shown on the left), such a variety of possible bonding configurations can generate multiple emission peaks (left inset). However, irradiation with an E_{22} resonant laser restructures the OCC, changing the pair of functional groups from the kinetic to thermodynamic configuration (e.g., from para to ortho bonding). As a result, the OCC PL emission narrows and blueshifts (insets).

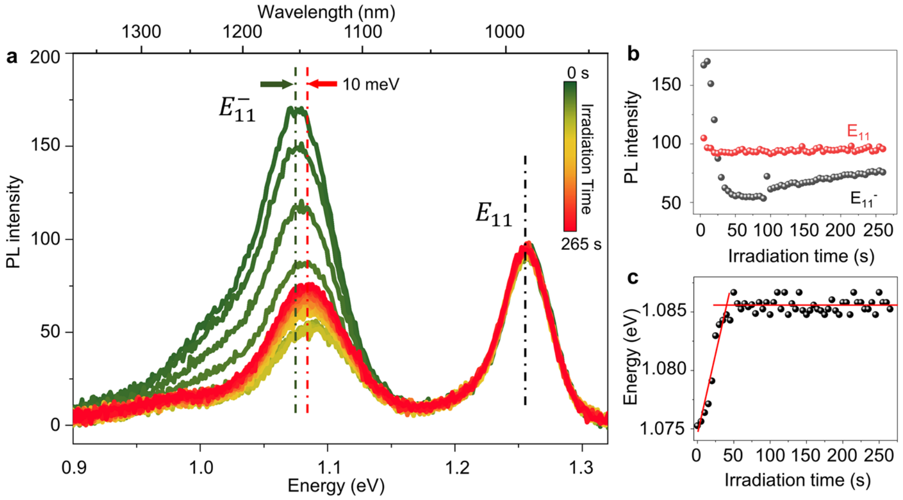

Figure 2. Spectral shifts in the OCC peak emission under light irradiation. (a) Ensemble PL measurements of OCC-(6,5)-SWCNTs dispersed in 2 w/v% DOC/H_2O solution and irradiated by 565 nm light at ∼10 mW/cm^2 for increasing time. Unlike the native SWCNT E_{11} emission peak at 988 nm, which remains unchanged, the OCC E_{11}^{-} wavelength shifts from ∼1153 to ∼1142 nm over 265 s of laser excitation. Additionally, the overall OCC emission intensity decreases. (b) Comparison of the E_{11} and E_{11}^{-} emission intensity as a function of the irradiation time. (c) Evolution of the E_{11}^{-} peak wavelength as a function of the irradiation time.

modified with diazonium chemistry, producing a broad distribution of OCC emission peaks in the range of 1100−1350 nm, even for the same functional groups on the same (6,5) chirality.[13] Previous work by us and others have shown that the bonding configurations can be reduced by choosing atomically symmetric SWCNT hosts (i.e., (*n*, 0) nanotubes),[18] divalent bonding groups,[5,20] or via thermal annealing (at 500 °C for over 80 min).[21] However, these methods only work for zigzag SWCNTs, which have a low abundance and purification yield,[22] or result in significant loss of the material (25−34% by weight) and substantial removal of OCCs from the SWCNT surfaces.[21] Furthermore, none of these approaches allow for localized control of the bonding configuration, which will be required to study the coupling effect of identical quantum defects. A method that can be generally applied to all semiconducting SWCNT hosts to reconfigure the defect structure, ideally locally so it could potentially be integrated with molecular patterning,[23] would provide a powerful means for controlling the atomic configuration and thus quantum emission and coupling of OCCs.[1,2]

Herein, we show that laser irradiation of OCC-SWCNTs can locally convert kinetic configurations of the OCC functional group pair to the more thermodynamically stable structure, leading to a single defect PL peak. This process is driven by a laser that resonantly excites the SWCNT host at its excitonic transition to promote local rearrangement of the OCC bonds while keeping the carbon lattice intact (Figure 1). We confirmed this structural transformation by measuring the change in the OCC PL at both the ensemble and individual nanotube levels, which show significantly narrowed distribution of the OCC emission peaks by ~26%. Density functional theory (DFT) and time-dependent DFT (TD-DFT) simulations suggest that OCCs with kinetic configurations transform into the more thermodynamically stable ortho structure upon laser irradiation, with the calculated spectral shifts resulting from this structural rearrangement in good agreement with the observed experimental trends. These findings demonstrate the feasibility to locally reconfigure OCCs, providing a possible synthetic approach to achieve identical quantum emitters.

RESULTS AND DISCUSSION

We synthesized model OCC-SWCNTs by covalently attaching 3,4,5-trifluoroaryl groups on CoMoCat (6,5)-SWCNTs using a scalable, aqueous diazonium chemistry[6] followed by purification (see Methods for more details). Excitation−emission PL mapping of the resulting OCC-(6,5)-SWCNT solution revealed three major peaks (Figure S1a), including the E_{11} PL of the nanotube host at ~987 nm and convoluted OCC PL bands centered at ~1150 nm (E_{11}^-), as well as a sideband extending from 1200 to ~1300−1400 nm, which we label as E_{11}^{-*}. These defect-induced emissions are broad and complex. However, we found that continuous irradiation of the OCC-(6,5)-SWCNT solution at room temperature with 565 nm light, which resonantly excites the E_{22} band of the (6,5)-SWCNT host (Figure S1b) and changes both the position and intensity of the OCC peaks (Figure 2a). Over the course of irradiating the sample (265 s), we observed two stages in the change of E_{11}^- in real time. During the first 50 s of irradiation, the intensity of the E_{11}^- emission decreased, followed by a gradual increase of the intensity (Figure 2b). Meanwhile, the E_{11}^- wavelength blueshifted from 1153 (1.075) to 1142 nm (1.085 eV) over the first 50 s and then stabilized at ~1142 nm (Figure 2c). Notably, the E_{11}^{-*} sideband centered at 1218 nm (1.018 eV), which can be better resolved by fitting the PL spectra with Voigt functions (Figure S2), disappeared after irradiation. We observed a similar reduction of E_{11}^{-*} with 4-nitroaryl OCCs on (6,4)-SWCNTs (Figure S3), suggesting this phenomenon may be generalizable to other chiralities and OCCs. However, in this work, we chose to focus on 3,4,5-trifluoaryl OCCs on (6,5)-SWCNTs as a model system, since 3,4,5-trifluoaryl is less prone to possible polymerization,[24] which can complicate the interpretation, while (6,5)-SWCNT is the most studied chirality in the literature.

To identify the reason behind these observed changes in the defect PL upon irradiation with 565 nm light, we first ruled out several possibilities. We note the 3,4,5-trifluoaryl group is resistant to further chemical reactions due to its strong C−F bonds,[24−26] making it unlikely that the OCC functional group itself has changed during the irradiation process. We further prevented ultraviolet (UV) photon-triggered side reactions[14,27−30] by removing the UV photons from the incident light source using a 400 nm long path filter. The irradiation of 565 nm light on pristine (6,5)-SWCNTs under our experimental condition does not generate defect emissions (Figure S4). We also coated the SWCNTs with sodium deoxycholate (DOC), a surfactant known to prevent other potential reactants in solution from gaining access to the graphitic surface. Furthermore, we removed the excess diazonium reactant by ultrafiltration. Other possibilities that may contribute to the observed defect PL include trions[31,32] and aryl-group-localized radical pairs.[33] Although our work does not fully rule out these possibilities, radicals from aryl OCC-tailored (6,5)-SWCNTs should be undetectable above 200 K.[33] Furthermore, we note that light-induced global heating effects should not be a major factor, as a previous study found the solution temperature remained nearly unchanged (within 0.6 °C) even after irradiating the sample using a 561 nm laser at ~1 W/cm^2 for 60 min.[34] Since the power density that we used here (Figure 2) is 100-times lower, we can conclude that the observed PL emission changes were not due to a global heating effect. Additionally, the stability of the E_{11} emission during irradiation further suggests that neither the endohedral nor exohedral environments of the nanotubes have changed.[35]

Having ruled out these other possibilities, we hypothesize the observed spectral changes of the OCCs are due to bonding reconfigurations triggered by the E_{22} resonant irradiation of the nanotube hosts. Excitation of the (6,5)-SWCNT E_{22} transition generates mobile excitons that are known to relax to the nanotube's lower E_{11} energy level, as shown in Figure S5. The intrinsic E_{11} emission displays a low quantum yield of just ~1%,[36] with ~99% of the absorbed photon energy lost to the dark states and releasing as heat that is expected to heat up the entire length of the nanotube. Alternatively, in the presence of OCCs, the E_{11} excitons can be efficiently channeled to these defect sites, where the excitons are trapped at the lower E_{11}^- or E_{11}^{-*} energy levels, with the difference in energy compared to the original E_{11} state of the mobile exciton being locally released as heat at the OCC sites.[19] Although we cannot rule out the possibility of an exciton-induced photoreaction that could cause reconfiguration of the OCC bonding, if this does occur, it will be a surprisingly rare example that is triggered by an exciton rather than direct excitation with a photon. For these reasons, we hypothesize that the thermal energy generated locally at the OCC sites (as opposed to the temperature of the bulk solution) could be sufficient to trigger rearrangement of different kinetically derived bonding configurations of the OCCs to fewer, more thermodynamically stable structures that would result in the observed narrower distribution of the defect PL peaks.

During irradiation, these less stable OCCs appear to rearrange in two steps into a more stable bonding configuration that emits at 1140 nm. The first step is evidenced by the decreasing intensity of the E_{11}^- and E_{11}^{-*} peaks during the first 50 s of irradiation, narrowing into a single E_{11}^- peak (Figure S2). The second step is characterized by the slow increase of the E_{11}^- intensity in addition to the peak's slight blueshifting (12 meV) upon continued 565 nm irradiation (>50 s) (Figure 2). These results suggest that the number of kinetic bonding configurations is reduced, eventually converging into the most thermodynamically stable structure, as exemplified by the single, narrowed, and somewhat blueshifted E_{11}^- emission peak that remains at the end of the irradiation process. This phenomenon could explain why E_{11}^- is typically observed as a major peak in OCC-functionalized (6,5)-SWCNTs synthesized by light-accelerated chemistries,[14,16] in which the kinetically stable OCCs may already be converted into thermodynamically stable OCCs.

To more directly follow the evolution of the OCC configuration, we conducted *in situ* hyperspectral PL imaging of individual OCC-(6,5)-SWCNTs deposited on a substrate (see Materials and Methods).[37] To separate the irradiation effect from the PL measurement, we performed laser irradiation at a relatively high-power density of 184 W/cm^2 using a 561 nm laser, which resonantly excites the E_{22} band of

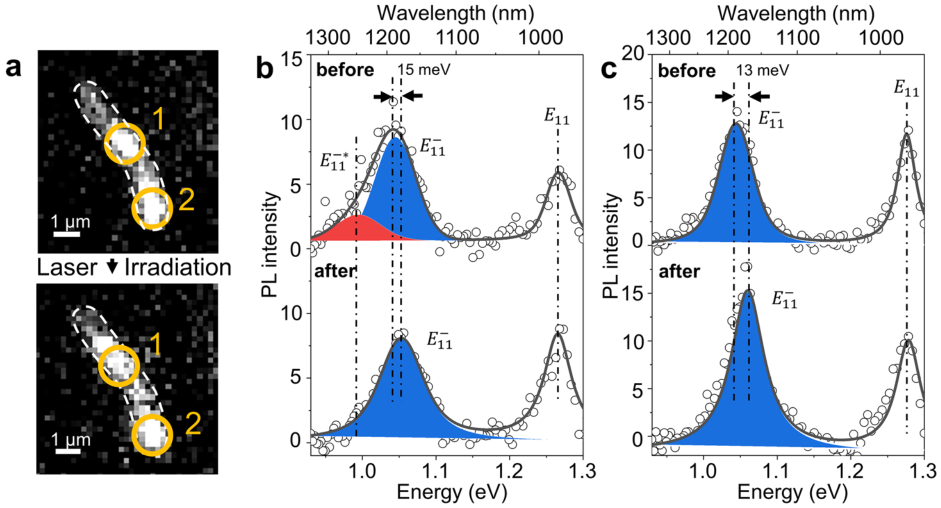

Figure 3. Changes in the PL of individual OCCs upon 561 nm laser irradiation. (a) PL images of an individual OCC-(6,5)-SWCNT before (top) and after (bottom) irradiating with a 561 nm laser at a power density of 184 W/cm^2 for 30 min. These PL images were taken with a 1100 nm long-pass filter and 730 nm excitation. (b) PL spectra from site 1 (shown in a) before (top) and after (bottom) irradiation, in which the $E_{11}^{-}*$ peak at 0.995 eV disappears while E_{11}^{-} blueshifts by 15 meV. (c) PL spectra from spot 2 (shown in a) before (top) and after (bottom) irradiation, in which the E_{11}^{-} emission blueshifts by 13 meV.

the (6,5)-SWCNT host. Then we probed the PL at a low power density of 42 W/cm^2 using a 730 nm laser, which off-resonantly excites the nanotubes without changing the OCCs (Figures S1b and S6). Figure 3a shows a PL image of an individual OCC-(6,5)-SWCNT with two OCC sites emitting at >1100 nm (1.13 eV) (indicated by the yellow circles) before and after 561 nm laser irradiation. The corresponding PL spectra from these two OCC sites before (top) and after (bottom) laser irradiation are shown in Figure 3b,c, respectively. At site 1, we observed two peaks in the initial OCC emission, E_{11}^{-} at 1187 nm (1.044 eV) and $E_{11}^{-}*$ at 1246 nm (0.995 eV). After irradiation for 30 min, the intensity of the $E_{11}^{-}*$ peak significantly decreased, while the E_{11}^{-} peak blueshifted to 1171 nm (1.059 eV). Figure 4 shows more examples of the blueshifted E_{11}^{-} peak and decrease of $E_{11}^{-}*$. Out of 91 nanotubes investigated, we observed a blueshift of 34−58 meV from $E_{11}^{-}*$ to E_{11}^{-} (Figures 4b−e and S7). Additionally, no further changes were observed after the first 30 min of irradiation (Figure 4c). These trends are consistent with our ensemble solution-based measurements (Figure 2). However, the spectra of individual emitting sites, as shown in Figure 3a, demonstrate the diverse OCC structures that can be generated by the diazonium chemistry. Unlike at site 1, where both E_{11}^{-} and $E_{11}^{-}*$ are present, site 2 only features the E_{11}^{-} peak, which blueshifts by 10 meV from 1124 (1.103) to 1114 nm (1.113 eV) upon laser irradiation (Figure 3c). Despite the observed spectral heterogeneity of the starting material, these findings further demonstrate the ability to modify the OCC emission wavelength by resonantly exciting the SWCNT host to predominantly achieve the E_{11}^{-} emission.

Additionally, as with the bulk measurements, the single-nanotube hyperspectral PL imaging showed the native E_{11} peak of the majority of OCC-(6,5)-SWCNTs remained nearly identical before and after irradiation (Figures 3, 4, and S7). Similarly, irradiating the pristine (6,5)-SWCNTs with 561 nm light caused no defect-induced emission peaks to appear and the position of the native E_{11} emission was maintained (Figure 4f). The stability of the E_{11} emission in the hyperspectral imaging experiments provides further evidence that the laser excitation does not add nor remove OCC defects on the SWCNTs in these nanotubes. Therefore, the observed shifts and changes in intensity of E_{11}^{-} and $E_{11}^{-}*$ are due to rearrangement of the OCC bonding configurations. We note in some rare cases (e.g., Figure 3b) the E_{11} intensity increases, while $E_{11}^{-}*$ disappears, suggesting the removal of these OCCs. We also note that these defects are often characterized by Raman scattering as well, as shown previously.[4] However, due to the sparse density of defects on each nanotube, our Raman instrument does not have the sensitivity to detect the change that provides an unambiguous correlation with our PL measurements.

We wanted to further explore the mechanism behind these observed PL shifts and intensity changes of the E_{11}^{-} and $E_{11}^{-}*$ peaks due to possible OCC bond rearrangement in the individual nanotube measurements. Once again, we were curious whether a global or local heating effect was the cause behind the observed shifts. During irradiation, we estimated that the nanotube temperature increased by less than 1 °C (Supplementary Note 1). Therefore, we can again exclude a global heating effect, which suggests that the observed OCC bonding rearrangement is instead triggered by the local thermal energy generated by exciton trapping and relaxation at the OCC sites.

We further performed the irradiation using the 561 nm laser at two different power densities (Figure 4d,e). Irradiating an individual SWCNT that predominantly showed $E_{11}^{-}*$ using the 561 nm laser at a power density of 37 mW/cm^2 caused the intensity of $E_{11}^{-}*$ to decrease while the E_{11}^{-} peak at 1142 nm (1.085 eV) appeared (Figure 4d). Similarly, an individual OCC-(6,5)-SWCNT showed the $E_{11}^{-}*$ intensity decreased while the E_{11}^{-} intensity increased after irradiation with 561 nm light at a power density of just 1 W/cm^2 for 30 min. Furthermore, we observed a gradual conversion of $E_{11}^{-}*$ to E_{11}^{-} when irradiated with 561 nm light at 184 W/cm^2 for 10−20 min (Figure S7). After 20 min irradiation, the $E_{11}^{-}*$ peak completely disappeared while the intensity of E_{11}^{-} increased, becoming the dominant OCC emission. Meanwhile, the intensity of E_{11} did not change, indicating no new OCC

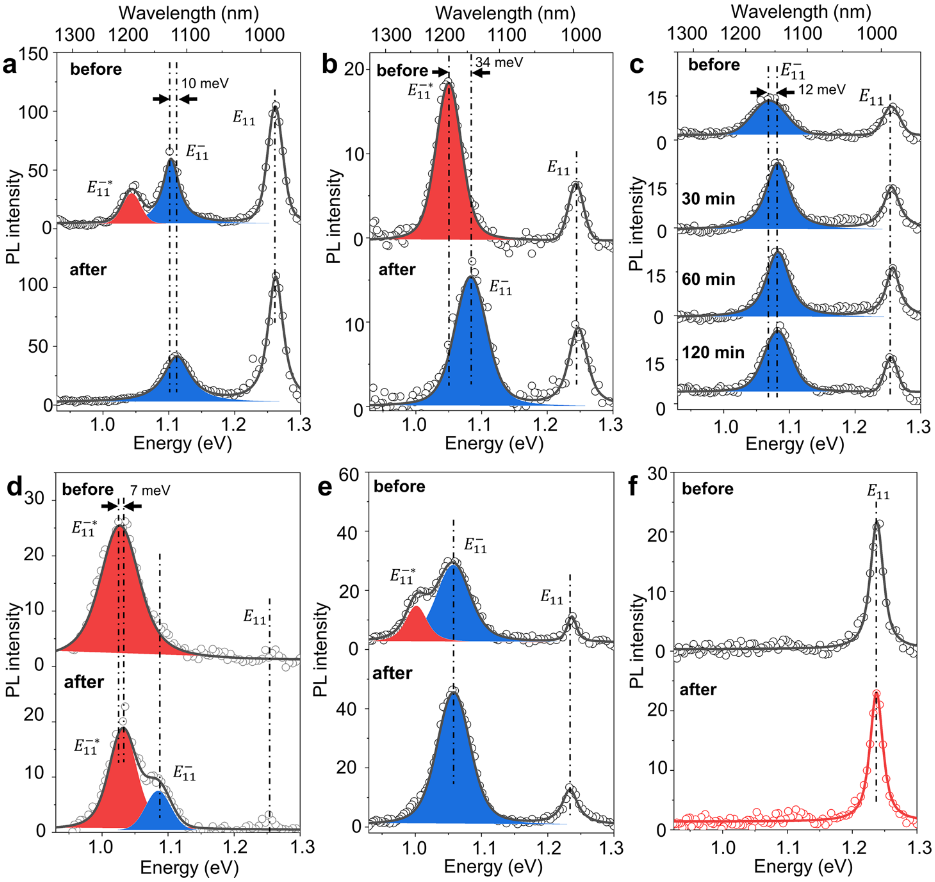

Figure 4. PL spectra of individual OCC-(6,5)-SWCNTs before and after laser irradiation. PL spectra of two individual OCC-(6,5)-SWCNTs (a,b) before (top) and after (bottom) irradiating with a 561 nm laser at a power density of 184 W/cm^2 for 30 min. (a) Irradiation removes E_{11}^{-}* at 1187 nm (1.044 eV), while E_{11}^{-} blueshifts by 10 meV, from 1124 (1.103) to 1114 nm (1.113 eV). (b) The blueshift of E_{11}^{-}* to E_{11}^{-} after laser irradiation was 34 meV, specifically from 1181 (1.050) to 1145 nm (1.083 eV). (c) PL spectra from an individual OCC-(6,5)-SWCNT before (top) and after (bottom) longer irradiation of up to 2 h using a 561 nm laser at a power density of 184 W/cm^2. These results demonstrated that under these conditions the OCC change occurs within the first 30 min and becomes stable after that. (d) PL spectra of an individual OCC-(6,5)-SWCNT predominantly featuring E_{11}^{-}* emission before (top) and after (bottom) irradiating with a 561 nm laser at a power density of ~37 mW/cm^2 for 30 min, which is comparable to the light power density of ~10 mW/cm^2 used in Figure 2. (e) PL spectra of an individual OCC-(6,5)-SWCNT featuring E_{11}^{-} and E_{11}^{-}* before (top) and after (bottom) irradiating with a 561 nm laser at a power density of ~1 W/cm^2 for 30 min. (f) The pristine (6,5)-SWCNT control shows that the irradiation process does not generate OCC defects nor does it cause structural damage to the nanotube host.

defects had been added or removed. These results further suggest that the irradiation process converts OCCs that emit at E_{11}^{-}* to that emits at E_{11}^{-}.

To better quantify the impact of laser irradiation on the OCC emission shifts, we statistically assessed the OCC peaks of 67 individual nanotubes (Figure 5). We found that the laser irradiation narrowed the OCC peak distribution by ~26%, reduced from 166 meV, which includes E_{11}^{-} (1129−1238 nm) and E_{11}^{-}* (1221−1330 nm), to 123 meV (1107−1245 nm) with E_{11}^{-} only. In general, we observed 3 types of nanotubes in terms of the change in their OCC emissions: (a) 38 out of the 67 nanotubes we measured exhibited only one OCC peak (E_{11}^{-}) and blueshifted by 9−34 meV after irradiation; (b) 23 of the 67 nanotubes showed both E_{11}^{-} and E_{11}^{-}* peaks, in which E_{11}^{-} blueshifted and E_{11}^{-}* diminished upon irradiation; (c) finally, OCCs from 6 of the nanotubes showed only E_{11}^{-} emission that remained stable (without shifting) upon laser irradiation (example is shown in Figure S8). This range of the E_{11}^{-} peak position even after irradiation can be attributed to the different environments of the nanotubes, both exterior and interior, in which the water molecules may partially evaporate from the SWCNT interiors at varying amounts (Supplementary Note 2).[35,38] It is also worth pointing out that low-temperature PL measurements[12] in combination with single-defect spectroscopy[37] may provide additional details on the evolution of these OCCs under laser irradiation, which requires future experiments. However, there is a clear trend from both ensemble and individual nanotube PL measurements suggesting that the OCC configuration changes from a kinetically derived structure to a more thermodynamically stable one upon irradiation with E_{22} resonant light.

To understand the configurational change of these quantum defects upon laser irradiation, we simulated the system energy of the OCC-SWCNTs using DFT calculations. We propose a naming convention to describe the rich structures afforded by these quantum defects, particularly OCC defect pairs. This naming system is inspired by the Miller index-like description of the sp^2 carbon lattice, which is widely used to distinguish the different (n, m) chiralities of tubular structures, such as carbon nanotubes and hexagonal boron nitride nanotubes, as well as graphene ribbons.[39] We define the position of the first defect as the origin, (0,0). The atomic configuration of an OCC can

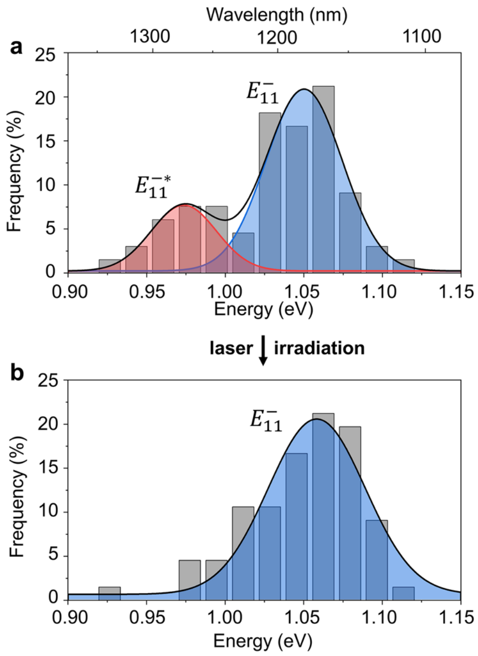

Figure 5. Statistical analysis of the OCC emission of 67 individual OCC-(6,5)-SWCNTs before and after laser irradiation. Histogram of the different E_{11}^- and E_{11}^{-*} emission energies observed of individual nanotubes (a) before and (b) after irradiating with a 561 nm laser at a power density of 184 W/cm^2 for 30 min. In total, 90 OCC peaks in these 67 (6,5)-SWCNTs were observed before irradiation, including 67 that featured the E_{11}^- peak and 23 that displayed E_{11}^{-*}. After irradiation, 13 of the E_{11}^{-*} peaks diminished and the number of OCC sites emitting at E_{11}^- increased by 6.

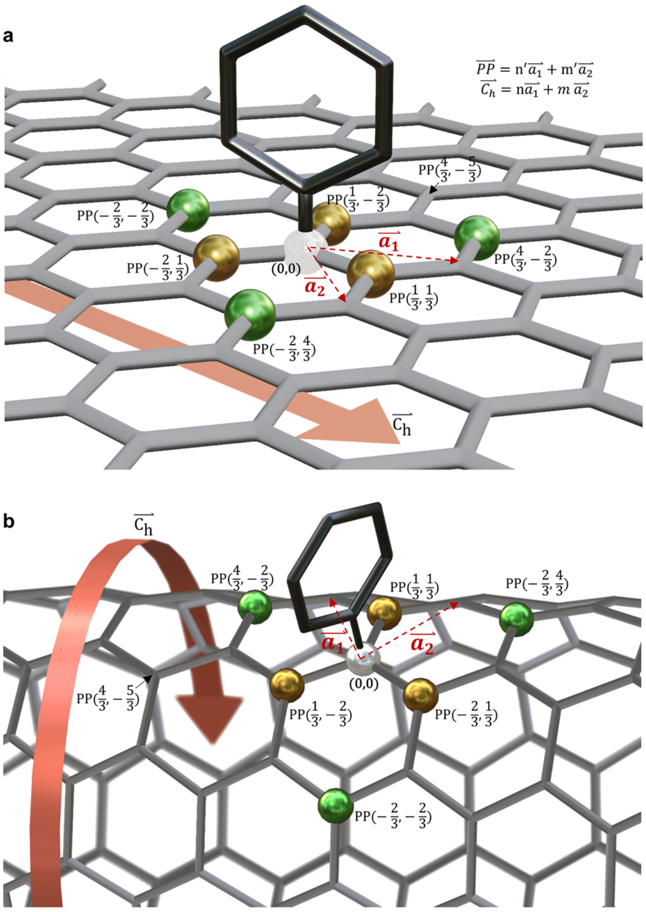

Figure 6. Naming system for the rich OCC bonding configurations. (a) Graphene sheet with an OCC that contains a pair of covalently attached functional groups. The bonding site for the first group ($-C_6H_5$ here) is defined as the origin of this coordinate system, and the carbon (gold and green atoms) for bonding the pairing group (H or −OH, not shown here) is defined by the pairing position (PP(n', m')). The corresponding pairing position vector is defined by $\overrightarrow{PP} = n'\vec{a}_1 + m'\vec{a}_2$, where $\vec{a}_1$ and $\vec{a}_2$ are the two basis vectors for the hexagonal sp^2 carbon lattice. The chiral vector $\vec{C}_h = n\vec{a}_1 + m\vec{a}_2$ for the nanotube host is also shown. (b) Molecular model for an OCC-tailored (6,5)-SWCNT which is rolled up from graphene following the chiral vector $\vec{C}_h$ in a. The pairing positions for the "ortho" configurations (green), including PP(1/3, −2/3), PP(−2/3, 1/3), and PP(1/3, 1/3), and the "para" configurations (gold), including PP(4/3, −2/3), PP(−2/3, −2/3), and PP(−2/3, 4/3), are indicated on the lattice.

then be uniquely determined by the pairing position, PP(x, y), which follows $\overrightarrow{PP(x, y)} = x\vec{a}_1 + y\vec{a}_2$ where $\vec{a}_1$ and $\vec{a}_2$ are the two base vectors for the sp^2 carbon lattice. With this naming system, we can identify each of the para and ortho defects, and any other atomic configuration, for a specific nanotube host. For example, an "ortho" defect can actually take up to three distinct atomic configurations, which can be differentiated as PP(1/3, 1/3), PP(1/3, −2/3), and PP(−2/3, 1/3) on a (6,5)-SWCNT host (Figure 6). Similarly, the "para" configurations[40,41] include PP(4/3, −2/3), PP(−2/3, −2/3), and PP(−2/3, 4/3). This naming system can be readily expanded to associate each atomic bonding position with the specific functional group along with the chirality of the nanotube host. A comparison of our naming system and existing ones[12,18] is shown in Table S1. We note that such a rich structural variability may also occur with other low dimensional materials such as transition metal dichalcogenides and graphene ribbons,[42−44] and this naming system can similarly be applied to this increasingly rich family of atomic defects on different hosts.

We modeled six different configurations that contained the 3,4,5-trifluoroaryl group at the center of a 12 nm long (6,5)-SWCNT and a pairing hydrogen group attached to the adjacent carbon atoms, including three ortho positions (PP(1/3, −2/3), PP(−2/3, 1/3), and PP(1/3, 1/3)) and three para positions (PP(4/3, −2/3), PP(−2/3, −2/3), and PP (−2/3, 4/3)), as shown in Figure 7. We performed the geometry optimization of each OCC-SWCNT structure and calculated the system energies (see Materials and Methods). The ortho PP(−2/3, 1/3) configuration resulted in the lowest system energy among the tested structures, indicating that it is the most thermodynamically stable bonding configuration. These results align with a previous simulation study by Tretiak and co-workers using H and 4-bromoaryl pairs as OCCs.[40] We found in our case that other configurations were 90−400 meV destabilized with respect to the ortho PP(−2/3, 1/3) position (Table 1). The difference in the total system energies suggest that the structural stability of the OCC-SWCNTs depends on the relative bonding configuration between the OCC and its pairing group. Furthermore, TD-DFT calculations confirm that each OCC bonding configuration produces an E_{11}^- emission 27−418 meV lower in energy compared to E_{11} (Table 1 and Figure S9).

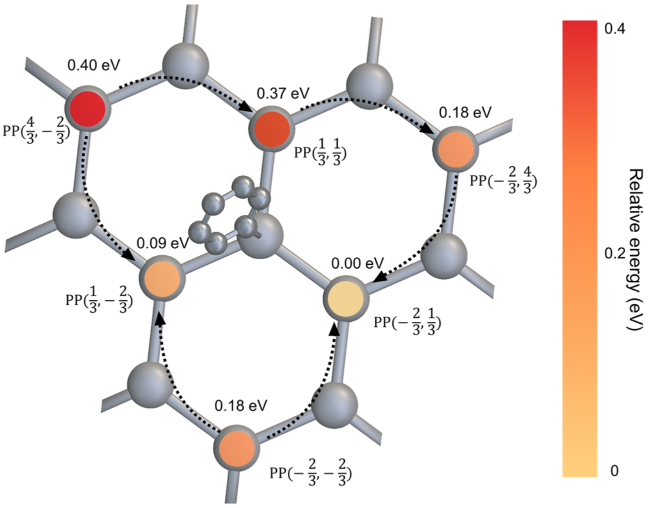

Figure 7. Relative energies of the different bonding configurations of an OCC composed of 3,4,5-trifluoroaryl and −H groups on a (6,5)-SWCNT. The 3,4,5-trifluoroaryl is attached to the center carbon (0, 0) position. The −H pairing group was then bonded at three ortho ((PP(1/3, 1/3), PP(−2/3, 1/3), and PP(1/3, −2/3)) and three para positions (PP(4/3, −2/3), PP(−2/3, 4/3), and PP(−2/3, −2/3)). The possible reconfiguration routes are shown as dashed arrows. The colored circles represent the relative energy of each bonding configuration, located at the carbon that bonds to the −H group. The color and the numbers labeled represent the relative system energy compared to the thermodynamically most stable bonding configuration, PP(−2/3, 1/3).

Table 1. Relative Energies of the Simulated Bonding Configurations

bonding configuration	relative system energy (eV)[a]	OCC emission energy (eV)
PP(−2/3, 1/3)	0	1.744
PP(1/3, −2/3)	0.0906	1.427
PP(1/3, 1/3)	0.3688	1.673
PP(−2/3, 4/3)	0.1839	1.771
PP(−2/3, −2/3)	0.1837	1.567
PP(4/3, −2/3)	0.3961	1.382

[a] Relative system energies are reported relative to the ortho PP(−2/3, 1/3) structure, which has the lowest energy.

To assign the experimentally observed OCC peak shifts, we correlated the system energy with the optical transition energy of each bonding configuration from DFT and TD-DFT, respectively, and identified possible routes of such rearrangement. In each OCC, the bond energy of C−H is weaker than that of the C(sp^3)−C(aryl) bond, and thus, we considered the transition of the OCC bonding configuration based on H migration on the sp^2 carbon lattice around the aryl group. The −H group was allowed to rearrange two carbons away each time, constituting the para to ortho transition and vice versa. Although the transition states between each bonding configuration were not simulated due to the high computational costs., the laser irradiation induced defect bond breakage and formation has been previously demonstrated with larger diameter SWCNTs.[45] Following this method, we consider the bonding reconfiguration occurring from higher energy configurations to lower energy ones until the lowest energy structure is reached (Figure 7). We then performed TD-DFT calculations and compared the difference in the emission energy between the initial and final OCC configurations to determine whether any of these values matched the experimentally observed spectral shifts.

With this approach, we identified eight thermodynamically favorable routes for bonding reconfiguration (Figure 7 and Table 2). Four of these eight routes, from higher energy structures including ortho PP(1/3, 1/3), para PP(−2/3, 4/3), para PP(−2/3, −2/3), and para PP(4/3, −2/3) to the lower energy configurations of ortho PP(−2/3, 1/3) and ortho PP(1/3, −2/3), reduce in system energy by 0.18−0.40 eV, which we used to find an assignment of the blueshifted OCC peaks. Specifically, the PP(1/3, 1/3) ortho configuration has previously been associated with the experimentally observed E_{11}^{-} emission at ∼1150 nm (1.078 eV),[18,20,46] which we found to blueshift upon laser irradiation. Based on our calculations, the transformation most likely occurs following the energy descending ortho PP(1/3, 1/3) → para PP(−2/3, 4/3) → ortho PP(−2/3, 1/3) route. In contrast, para PP(−2/3, 4/3) → ortho PP(−2/3, 1/3) would result in red-shifted OCC emissions, which were not observed experimentally, suggesting para PP(−2/3, 4/3) OCCs are rarely formed during the OCC synthesis, which is consistent with a previous study by Tretiak, Doorn, and co-workers.[18] Para PP(−2/3, −2/3) can directly convert to ortho PP(−2/3, 1/3), also leading to a blueshift in its emission based on our calculations. Alternatively, para PP(−2/3, −2/3) can convert to ortho PP(1/3, −2/3), however, it would lead to a redshift in its emission based on TD-DFT calculations, which we did not observe experimentally.

Table 2. Proposed Routes for Bonding Reconfigurations

route of bonding reconfiguration	relative energy change[a] (eV)	change in OCC emission
PP(1/3, 1/3) → PP(−2/3, 4/3) → PP(−2/3, 1/3)	−0.3788	blueshift
PP(4/3, −2/3) → PP(1/3, 1/3) → PP(−2/3, 4/3) → PP(−2/3, 1/3)	−0.3961	blueshift
PP(4/3, −2/3) → PP(1/3, −2/3)	−0.3055	blueshift
PP(−2/3, −2/3) → PP(−2/3, 1/3)	−0.1837	blueshift
PP(−2/3, −2/3) → PP(1/3, −2/3)	−0.0931	redshift
PP(−2/3, 4/3) → PP(−2/3, 1/3)	−0.1839	redshift
PP(−2/3, 1/3) → PP(−2/3, 1/3)	0	none
PP(1/3, −2/3) → PP(1/3, −2/3)	0	none

[a] Relative energy change = the relative system energy of the final bonding configuration − the relative system energy of the initial bonding configuration.

From our experiments, we also observed the intensity of E_{11}^{-*} emitting in the range of 1221−1330 nm (0.932−1.015 eV) reduced upon laser irradiation. We speculate that this E_{11}^{-*} peak is related to PP(1/3, −2/3), whose emission occurs at a longer wavelength compared to E_{11}^{-} (<1.0 eV after correction according to previous study[47]) based on our TD-DFT calculation. Upon irradiation, this E_{11}^{-*} peak disappears, suggesting its associated bonding configuration is eliminated or rearranges to nonemissive structures, such as PP(4/3, −5/3) (shown in Figure 6) or even further to more than 3 carbon atoms away from the aryl site.[48] However, the nonemissive structure PP(4/3, −5/3) has a much higher relative energy of ∼1.58 eV compared to the para and other bonding configurations, making it inaccessible under our experimental conditions.

Taken together, our simulation and experimental observations suggest the bonding configurations synthesized before laser irradiation can be ortho configurations of PP(1/3, 1/3), PP(1/3, −2/3), and PP (−2/3, 1/3) and para configurations of PP(4/3, −2/3) and PP(−2/3, −2/3), with different thermodynamic stability. However, after laser irradiation, most of the kinetic configurations convert to the thermodynamically stable ortho PP(−2/3, 1/3) configuration, resulting in the observed single PL peak at a blueshifted wavelength.

CONCLUSIONS

The chemical synthesis of OCCs on the sp^2 carbon lattice of a SWCNT host creates many bonding configurations that result in a broad distribution of the quantum defect PL peaks. We show that resonant excitation of the nanotube host with light can convert the kinetic bonding structures to the thermodynamically stable configuration, leading to a single PL peak. We followed this structural reconfiguration on 3,4,5-trifluoroaryl OCC-tailored (6,5)-SWCNTs as a model system using *in situ* ensemble spectroscopy as well as single nanotube hyperspectral PL imaging. The results suggest the initially generated OCCs tend to form kinetically favorably though thermodynamically less stable bonding configurations during synthesis but can be removed or transformed into a more thermodynamically stable form by laser irradiation using a wavelength resonant with the E_{22} transition of the nanotube host. We also performed DFT simulations to reveal the possible pathways for the OCC conversion from the kinetic structures to the thermodynamically stable one. This study provides a synthetic route to control the atomic configurations of OCCs on sp^2 carbon lattices, which may ultimately enable the synthesis of identical quantum light sources for quantum information science, molecular sensing, and bioimaging.

MATERIALS AND METHODS

Synthesis of OCCs. We synthesized 3,4,5-trifluorobenzenediazonium tetrafluoroborate and 4-nitrobenzenediazonium tetrafluoroborate from 3,4,5-trifluoroanaline and 4-nitroaniline, respectively (Sigma-Aldrich) as previously described.[4] In brief, 3.0 mL of nanopure water and 2.6 mL of tetrafluoroboric acid solution (48 wt % in water, Sigma-Aldrich) were added to a round-bottom flask (RBF) which was then cooled in an ice bath. To the cooled RBF was added 4.8 mmol of aniline. We then dissolved 9.71 mmol of sodium nitrite (Sigma-Aldrich, ≥ 97.0%) in 2 mL of nanopure water, which was added dropwise to the RBF with stirring. The precipitated tetrafluoroborate salt was washed with 200 mL of diethyl ether under vacuum filtration for ∼20 min while being protected from light.

We synthesized the OCCs on semiconducting SWCNTs based on a method described in our previous work.[6] In brief, 0.020 mg of raw SWCNTs (CoMoCat SG65i) were dissolved in 1 mL of chlorosulfonic acid (Sigma-Aldrich, 99%) followed by the addition of ∼100 μL of 3,4,5-trifluorobenzenediazonium tetrafluoroborate (∼4 mg/mL) in chlorosulfonic acid. In the case of 4-nitrobenzenediazonium tetrafluoroborate, a low [diazonium salt]:[C] ratio of ∼1:2000 was used to minimize potential branching reactions on the OCC benzene ring. The SWCNT/acid mixture was then added drop-by-drop to nanopure water while stirring vigorously using a Teflon-coated magnetic stir bar. (***Safety Note: This reaction process aggressively generates heat and acidic smog. The experiment should be performed in a fume hood with proper personal protective equipment, including goggles/facial mask, lab coat, and acid-resistant gloves.***) The resulting SWCNTs subsequently precipitated out of the solution and were collected on a polyvinylidene fluoride membrane (MilliporeSigma VVLP membrane, 0.1 μm pore size) and then rinsed with ∼50 mL of Nanopure water. The product was a powder of OCC-SWCNTs, which was then dried in a vacuum oven at room temperature overnight.

Individual Dispersion of Long OCC-SWCNTs. The dry OCC-SWCNT powder was dispersed in a 2% (w/v) DOC (Sigma-Aldrich, >97%) aqueous solution by superacid−surfactant exchange.[6,49] Briefly, the OCC-SWCNT dry power was dissolved in chlorosulfonic acid to obtain a 0.02 mg/mL solution. We then added ∼2 mL of the OCC-SWCNT/chlorosulfonic acid solution drop-by-drop into 320 mL of NaOH (0.75 M) containing ∼0.08% (w/v) DOC aqueous solution with vigorous stirring until a pH of ∼8 was reached to obtain a black or gray solution of SWCNTs. The solution was stirred for at least another 30 min followed by the addition of several drops of concentrated HCl to protonate the DOC surfactant molecules, which coalesce into a gray precipitate along with the wrapped SWCNTs. The precipitate was filtered with a polyvinylidene fluoride filtration membrane (MilliporeSigma SVLP membrane 5 μm pore size). Then ∼12.8 mL of nanopure water and several drops of 1 M NaOH were added to the precipitate and the solution pH was tuned to ∼7−8. The mixture was further stirred for at least 1 day followed by centrifugation at ∼25 000 g for 90 min (Eppendorf centrifuge 5417R) to remove any undissolved SWCNT bundles. The average length of these nanotubes as described[49] is ∼1.3 μm.

Purification of OCC-Tailored (6,5)-SWCNTs. We adapted the aqueous two-phase extraction (ATPE) method[22,50] with some modifications to generate a chirality-sorted solution of OCC-(6,5)-SWCNTs. In detail, we first mixed 1 mL of the OCC-SWCNT aqueous solution dispersed by 2% (w/v) DOC (obtained after the superacid−surfactant exchange) with 0.3 mL of 50% (w/w) polyethylene glycol (PEG) (M.W. 6000 Da, Alfa Aesar) aqueous solution and 0.3 mL of 20% (w/w) dextran (M.W. 70000 Da, TCI) aqueous solution using a vortex mixer, followed by centrifugation (Eppendorf centrifuge 5810R) at 4000 g for 1 min to induce phase separation, in which the OCC-SWCNTs preferentially stay at the bottom phase (dextran rich). The DOC surfactants were then gradually exchanged to 0.9% (w/w) sodium cholate and 0.7% (w/w) sodium dodecyl sulfate (SDS) according to a published procedure.[50] Then ∼20 μL of 1 M NaSCN (99%, Sigma-Aldrich) solution was added as the phase modifier to induce metallic/semiconducting OCC-SWCNT sorting. After centrifuging the solution at 4000 g for 1 min, the OCC-(6,5)-SWCNTs preferentially stay at the top PEG-rich phase. The OCC-(6,5)-SWCNT solution was then pipetted out followed by centrifugal ultrafiltration (Amicon Ultra-15, 100 kDa) to remove the PEG polymers and residual diazonium salts. An ∼13 mL portion of 2% (w/v) DOC in H_2O was used to rinse the OCC-(6,5)-SWCNT solution 5 times during the ultrafiltration, resulting in the OCC-(6,5)-SWCNTs dispersed in 2% (w/v) DOC/H_2O.

Ensemble Spectroscopy Characterization. The ensemble PL spectra were collected with a NanoLog spectrofluorometer (Horiba Jobin Yvon). The samples were excited with a 450 W xenon source dispersed by a double-grating monochromator. The power density of the 565 nm light was ∼10 mW/cm^2. The slit width of the excitation and emission beams were 10 and 20 nm, respectively. A 400 nm long-pass filter (FGL400S, Thorlabs) was installed in the excitation pathway to remove the potential UV light. The PL spectra were collected using a liquid-N_2 cooled linear InGaAs array detector. The emission spectra were collected with excitation light at the E_{22} wavelength (565 nm for (6,5)-SWCNTs). The integration time to collect each spectrum was set to 0.01 s to minimize any change in the OCCs by light irradiation. Thus, during the collection of the PL spectra, the SWCNT samples were at most excited for 0.02 s. Each spectrum was taken *in situ* immediately after irradiating the nanotube solution with 565 nm light from the spectrofluorometer for 5 s, which added up to a total of 265 s. Note that all samples had an optical density (OD) of less than 0.5 at the (6,5) E_{11} band, measured using a PerkinElmer Lambda 1050 spectrophotometer with a broadband InGaAs detector.

Hyperspectral Imaging. To collect single nanotube PL images, 5 μL of the OCC-(6,5)-SWCNTs in 2% w/v DOC/D_2O solution was spin-coated at 3000 rpm for 1 min onto a ∼150 nm thick polystyrene layer on top of a ∼50 nm-thick Au layer on an Si substrate. The polystyrene layer acted as an insulating layer to prevent the SWCNTs from contacting with the Au, which would quench the PL. The Au layer was added as a mirror to double the excitation and emission light. The hyperspectral imaging was performed on a custom-built microscope.[40] We used an infrared optimized 100× objective (LCPLN100XIR, numerical aperture = 0.85, Olympus) along with a continuous wave laser at 730 nm (Shanghai Dream Lasers Technology Co., Ltd., power density of 42 W/cm^2) as the excitation light source for obtaining the PL spectra, as well as a 561 nm laser (JiveTM Cobolt AB, Sweden, power density of 341.79 W/cm^2) with a neutral density filter (Edmund Optics, OD 0.3, OD 0.9, OD 2.5 and OD 4.0.) to adjust the power density for irradiating the SWCNTs. The excitation power density at the sample was measured with an optical power meter (Newport 1916-C) and silicon detector (Newport 918-SLOD3). We note that the power density reported here does not consider the mirror effect of the Au layer, which may double the power density. Fluorescent emission from the sample was filtered through a long-pass dichroic mirror (875 nm edge, Semrock, USA) to remove the elastic laser scattering and then dispersed by a volume Bragg grating (Photon Etc, Inc. Montreal, Canada). Only the diffracted light with a narrow bandwidth of 3.7 nm was collected on the detector to form a spectral image. The PL spectra were fitted by Voigt profiles. Note the PL images of the OCC emissions in Figure 3a are taken with a 1100 nm long-pass filter (FELH1100, Thorlabs).

DFT and TD-DFT Calculations. All DFT calculations were performed with Gaussian 09 software.[51] We built OCC models by implanting a pair of groups (3,4,5-trifluoroaryl and hydrogen) in the center of a 12 nm (6,5)-SWCNT in three ortho and three para positions, as shown in Figure 7. The geometries of all structures were optimized using the Coulomb-attenuated B3LYP (CAM-B3LYP) functional[52] and 3-21G basis set.[53] This methodology has been successfully implemented previously by Gifford et al. to calculate optical transitions of functionalized SWCNTs.[40] The optical transitions were computed using TD-DFT with the same functional and basis set as in DFT. We analyzed the natural transition orbitals (NTOs)[54] with Gaussian 09 software and confirmed that the NTOs were strongly localized at the OCC, further verifying the defect origin of the optical transitions (Figure S10). We note the simulated peaks are higher in energy compared to the experimental data due to the vacuum environment used in the simulation and finite length of the SWCNTs. However, we did not correct the simulated peaks against experimental spectral data as proposed by Tretiak and co-workers[47] since this correction is a qualitative adjustment and does not change the relative emission energy ordering of the OCCs with different bonding configurations.

ASSOCIATED CONTENT

Supporting Information

The Supporting Information is available free of charge at https://pubs.acs.org/doi/10.1021/acsnano.1c07669.

> Supplementary notes, additional ensemble PL spectra and excitation−emission maps, UV−vis-NIR absorption spectra, hyperspectral PL spectra, DFT simulated OCC optical transitions, and NTO orbitals (PDF)

AUTHOR INFORMATION

Corresponding Author

YuHuang Wang − *Department of Chemistry and Biochemistry, University of Maryland, College Park, Maryland 20742, United States;* orcid.org/0000-0002-5664-1849; Email: yhw@umd.edu

Authors

Haoran Qu − *Department of Chemistry and Biochemistry, University of Maryland, College Park, Maryland 20742, United States;* orcid.org/0000-0003-4536-6703

Xiaojian Wu − *Department of Chemistry and Biochemistry, University of Maryland, College Park, Maryland 20742, United States*

Jacob Fortner − *Department of Chemistry and Biochemistry, University of Maryland, College Park, Maryland 20742, United States*

Mijin Kim − *Department of Chemistry and Biochemistry, University of Maryland, College Park, Maryland 20742, United States*

Peng Wang − *Department of Chemistry and Biochemistry, University of Maryland, College Park, Maryland 20742, United States*

Complete contact information is available at: https://pubs.acs.org/10.1021/acsnano.1c07669

Notes

The authors declare no competing financial interest.

ACKNOWLEDGMENTS

This work is supported in part by the National Science Foundation (grant no. CHE1904488). We also gratefully acknowledge the Maryland Advanced Research Computing Center (MARCC) for providing part of the computational resources for the quantum chemical calculations.

REFERENCES

(1) Brozena, A. H.; Kim, M.; Powell, L. R.; Wang, Y. Controlling the Optical Properties of Carbon Nanotubes with Organic Colour-Centre Quantum Defects. *Nat. Rev. Chem.* **2019**, *3*, 375−392.

(2) Gifford, B. J.; Kilina, S.; Htoon, H.; Doorn, S. K.; Tretiak, S. Controlling Defect-State Photophysics in Covalently Functionalized Single-Walled Carbon Nanotubes. *Acc. Chem. Res.* **2020**, *53*, 1791−1801.

(3) Shiraki, T.; Miyauchi, Y.; Matsuda, K.; Nakashima, N. Carbon Nanotube Photoluminescence Modulation by Local Chemical and Supramolecular Chemical Functionalization. *Acc. Chem. Res.* **2020**, *53*, 1846−1859.

(4) Piao, Y.; Meany, B.; Powell, L. R.; Valley, N.; Kwon, H.; Schatz, G. C.; Wang, Y. Brightening of Carbon Nanotube Photoluminescence through the Incorporation of sp3 Defects. *Nat. Chem.* **2013**, *5*, 840−845.

(5) Kwon, H.; Furmanchuk, A.; Kim, M.; Meany, B.; Guo, Y.; Schatz, G. C.; Wang, Y. Molecularly Tunable Fluorescent Quantum Defects. *J. Am. Chem. Soc.* **2016**, *138*, 6878−6885.

(6) Luo, H. B.; Wang, P.; Wu, X.; Qu, H.; Ren, X.; Wang, Y. One-Pot, Large-Scale Synthesis of Organic Color Center-Tailored Semiconducting Carbon Nanotubes. *ACS Nano* **2019**, *13*, 8417−8424.

(7) Kim, M.; Wu, X.; Ao, G.; He, X.; Kwon, H.; Hartmann, N. F.; Zheng, M.; Doorn, S. K.; Wang, Y. Mapping Structure-Property Relationships of Organic Color Centers. *Chem.* **2018**, *4*, 2180−2191.

(8) Ma, X.; Hartmann, N. F.; Baldwin, J. K.; Doorn, S. K.; Htoon, H. Room-Temperature Single-Photon Generation from Solitary Dopants of Carbon Nanotubes. *Nat. Nanotechnol.* **2015**, *10*, 671−675.

(9) He, X.; Hartmann, N. F.; Ma, X.; Kim, Y.; Ihly, R.; Blackburn, J. L.; Gao, W.; Kono, J.; Yomogida, Y.; Hirano, A.; Tanaka, T.; Kataura, H.; Htoon, H.; Doorn, S. K. Tunable Room-Temperature Single-Photon Emission at Telecom Wavelengths from sp3 Defects in Carbon Nanotubes. *Nat. Photonics* **2017**, *11*, 577−582.

(10) Luo, Y.; He, X.; Kim, Y.; Blackburn, J. L.; Doorn, S. K.; Htoon, H.; Strauf, S. Carbon Nanotube Color Centers in Plasmonic Nanocavities: A Path to Photon Indistinguishability at Telecom Bands. *Nano Lett.* **2019**, *19*, 9037−9044.

(11) Gisin, N.; Thew, R. Quantum Communication. *Nat. Photonics* **2007**, *1*, 165−171.

(12) He, X.; Gifford, B. J.; Hartmann, N. F.; Ihly, R.; Ma, X.; Kilina, S. V.; Luo, Y.; Shayan, K.; Strauf, S.; Blackburn, J. L.; Tretiak, S.; Doorn, S. K.; Htoon, H. Low-Temperature Single Carbon Nanotube Spectroscopy of Sp3 Quantum Defects. *ACS Nano* **2017**, *11*, 10785−10796.

(13) He, X.; Sun, L.; Gifford, B. J.; Tretiak, S.; Piryatinski, A.; Li, X.; Htoon, H.; Doorn, S. K. Intrinsic Limits of Defect-State Photoluminescence Dynamics in Functionalized Carbon Nanotubes. *Nanoscale* **2019**, *11*, 9125−9132.

(14) Wu, X.; Kim, M.; Kwon, H.; Wang, Y. Photochemical Creation of Fluorescent Quantum Defects in Semiconducting Carbon Nanotube Hosts. *Angew. Chem., Int. Ed. Engl.* **2018**, *57*, 648−653.

(15) Berger, F. J.; Luttgens, J.; Nowack, T.; Kutsch, T.; Lindenthal, S.; Kistner, L.; Muller, C. C.; Bongartz, L. M.; Lumsargis, V. A.; Zakharko, Y.; Zaumseil, J. Brightening of Long, Polymer-Wrapped Carbon Nanotubes by Sp3 Functionalization in Organic Solvents. *ACS Nano* **2019**, *13*, 9259−9269.

(16) Powell, L. R.; Piao, Y.; Wang, Y. Optical Excitation of Carbon Nanotubes Drives Localized Diazonium Reactions. *J. Phys. Chem. Lett.* **2016**, *7*, 3690−3694.

(17) Schmidt, G.; Gallon, S.; Esnouf, S.; Bourgoin, J. P.; Chenevier, P. Mechanism of the Coupling of Diazonium to Single-Walled Carbon Nanotubes and Its Consequences. *Chem.—Eur. J.* **2009**, *15*, 2101−2110.

(18) Saha, A.; Gifford, B. J.; He, X.; Ao, G.; Zheng, M.; Kataura, H.; Htoon, H.; Kilina, S.; Tretiak, S.; Doorn, S. K. Narrow-Band Single-Photon Emission through Selective Aryl Functionalization of Zigzag Carbon Nanotubes. *Nat. Chem.* **2018**, *10*, 1089−1095.

(19) Kim, M.; Adamska, L.; Hartmann, N. F.; Kwon, H.; Liu, J.; Velizhanin, K. A.; Piao, Y.; Powell, L. R.; Meany, B.; Doorn, S. K.; Tretiak, S.; Wang, Y. Fluorescent Carbon Nanotube Defects Manifest Substantial Vibrational Reorganization. *J. Phys. Chem. C* **2016**, *120*, 11268−11276.

(20) Gifford, B. J.; He, X.; Kim, M.; Kwon, H.; Saha, A.; Sifain, A. E.; Wang, Y.; Htoon, H.; Kilina, S.; Doorn, S. K.; Tretiak, S. Optical Effects of Divalent Functionalization of Carbon Nanotubes. *Chem. Mater.* **2019**, *31*, 6950−6961.

(21) Maeda, Y.; Murakoshi, H.; Tambo, H.; Zhao, P.; Kuroda, K.; Yamada, M.; Zhao, X.; Nagase, S.; Ehara, M. Thermodynamic Control of Quantum Defects on Single-Walled Carbon Nanotubes. *Chem. Commun.* **2019**, *55*, 13757−13760.

(22) Ao, G.; Khripin, C. Y.; Zheng, M. DNA-Controlled Partition of Carbon Nanotubes in Polymer Aqueous Two-Phase Systems. *J. Am. Chem. Soc.* **2014**, *136*, 10383−10392.

(23) Huang, Z.; Powell, L. R.; Wu, X.; Kim, M.; Qu, H.; Wang, P.; Fortner, J. L.; Xu, B.; Ng, A. L.; Wang, Y. Photolithographic Patterning of Organic Color-Centers. *Adv. Mater.* **2020**, *32*, e1906517.

(24) Salice, P.; Fabris, E.; Sartorio, C.; Fenaroli, D.; Figà, V.; Casaletto, M. P.; Cataldo, S.; Pignataro, B.; Menna, E. An Insight into the Functionalisation of Carbon Nanotubes by Diazonium Chemistry: Towards a Controlled Decoration. *Carbon* **2014**, *74*, 73−82.

(25) Combellas, C.; Kanoufi, F.; Pinson, J.; Podvorica, F. I. Time-of-Flight Secondary Ion Mass Spectroscopy Characterization of the Covalent Bonding between a Carbon Surface and Aryl Groups. *Langmuir* **2005**, *21*, 280−286.

(26) Greenwood, J.; Phan, T. H.; Fujita, Y.; Li, Z.; Ivasenko, O.; Vanderlinden, W.; Van Gorp, H.; Frederickx, W.; Lu, G.; Tahara, K.; Tobe, Y.; Uji-i, H.; Mertens, S. F. L.; De Feyter, S. Covalent Modification of Graphene and Graphite Using Diazonium Chemistry: Tunable Grafting and Nanomanipulation. *ACS Nano* **2015**, *9*, 5520−5535.

(27) Ghosh, S.; Bachilo, S. M.; Simonette, R. A.; Beckingham, K. M.; Weisman, R. B. Oxygen Doping Modifies near-Infrared Band Gaps in Fluorescent Single-Walled Carbon Nanotubes. *Science* **2010**, *330*, 1656−1659.

(28) Iakoubovskii, K.; Minami, N.; Kim, Y.; Miyashita, K.; Kazaoui, S.; Nalini, B. Midgap Luminescence Centers in Single-Wall Carbon Nanotubes Created by Ultraviolet Illumination. *Appl. Phys. Lett.* **2006**, *89*, 173108.

(29) Zheng, Y.; Bachilo, S. M.; Weisman, R. B. Photoexcited Aromatic Reactants Give Multicolor Carbon Nanotube Fluorescence from Quantum Defects. *ACS Nano* **2020**, *14*, 715−723.

(30) Kozawa, D.; Wu, X.; Ishii, A.; Fortner, J.; Otsuka, K.; Xiang, R.; Inoue, T.; Maruyama, S.; Wang, Y.; Kato, Y. K. Formation of Organic Color Centers in Air-Suspended Carbon Nanotubes Using Vapor-Phase Reaction. *arXiv.org*; 2021; 2103.00689; https://www.arxiv.org/abs/2103.00689.

(31) Brozena, A. H.; Leeds, J. D.; Zhang, Y.; Fourkas, J. T.; Wang, Y. Controlled Defects in Semiconducting Carbon Nanotubes Promote Efficient Generation and Luminescence of Trions. *ACS Nano* **2014**, *8*, 4239−4247.

(32) Kwon, H.; Kim, M.; Nutz, M.; Hartmann, N. F.; Perrin, V.; Meany, B.; Hofmann, M. S.; Clark, C. W.; Htoon, H.; Doorn, S. K.; Hogele, A.; Wang, Y. Probing Trions at Chemically Tailored Trapping Defects. *ACS Cent. Sci.* **2019**, *5*, 1786−1794.

(33) Lohmann, S. H.; Trerayapiwat, K. J.; Niklas, J.; Poluektov, O. G.; Sharifzadeh, S.; Ma, X. sp3-Functionalization of Single-Walled Carbon Nanotubes Creates Localized Spins. *ACS Nano* **2020**, *14*, 17675−17682.

(34) Wang, C.; Meany, B.; Wang, Y. Optically Triggered Melting of DNA on Individual Semiconducting Carbon Nanotubes. *Angew. Chem., Int. Ed. Engl.* **2017**, *56*, 9326−9330.

(35) Qu, H.; Rayabharam, A.; Wu, X.; Wang, P.; Li, Y.; Fagan, J.; Aluru, N. R.; Wang, Y. Selective Filling of N-Hexane in a Tight Nanopore. *Nat. Commun.* **2021**, *12*, 310.

(36) Crochet, J.; Clemens, M.; Hertel, T. Quantum Yield Heterogeneities of Aqueous Single-Wall Carbon Nanotube Suspensions. *J. Am. Chem. Soc.* **2007**, *129*, 8058−8059.

(37) Wu, X.; Kim, M.; Qu, H.; Wang, Y. Single-Defect Spectroscopy in the Shortwave Infrared. *Nat. Commun.* **2019**, *10*, 2672.

(38) Cambre, S.; Wenseleers, W. Separation and Diameter-Sorting of Empty (End-Capped) and Water-Filled (Open) Carbon Nanotubes by Density Gradient Ultracentrifugation. *Angew. Chem., Int. Ed. Engl.* **2011**, *50*, 2764−2768.

(39) Dresselhaus, M. S.; Dresselhaus, G.; Saito, R. Physics of Carbon Nanotubes. *Carbon* **1995**, *33*, 883−891.

(40) Gifford, B. J.; Kilina, S.; Htoon, H.; Doorn, S. K.; Tretiak, S. Exciton Localization and Optical Emission in Aryl-Functionalized Carbon Nanotubes. *J. Phys. Chem. C* **2018**, *122*, 1828−1838.

(41) Niyogi, S.; Hamon, M. A.; Hu, H.; Zhao, B.; Bhowmik, P.; Sen, R.; Itkis, M. E.; Haddon, R. C. Chemistry of Single-Walled Carbon Nanotubes. *Acc. Chem. Res.* **2002**, *35*, 1105−1113.

(42) Manzeli, S.; Ovchinnikov, D.; Pasquier, D.; Yazyev, O. V.; Kis, A. 2d Transition Metal Dichalcogenides. *Nat. Rev. Mater.* **2017**, *2*, 17033.

(43) Choi, W.; Choudhary, N.; Han, G. H.; Park, J.; Akinwande, D.; Lee, Y. H. Recent Development of Two-Dimensional Transition Metal Dichalcogenides and Their Applications. *Mater. Today* **2017**, *20*, 116−130.

(44) Celis, A.; Nair, M. N.; Taleb-Ibrahimi, A.; Conrad, E. H.; Berger, C.; de Heer, W. A.; Tejeda, A. Graphene Nanoribbons: Fabrication, Properties and Devices. *J. Phys. D: Appl. Phys.* **2016**, *49*, 143001.

(45) Souza, N.; Zeiger, M.; Presser, V.; Mücklich, F. In Situ Tracking of Defect Healing and Purification of Single-Wall Carbon Nanotubes with Laser Radiation by Time-Resolved Raman Spectroscopy. *RSC Adv.* **2015**, *5*, 62149−62159.

(46) Settele, S.; Berger, F. J.; Lindenthal, S.; Zhao, S.; El Yumin, A. A.; Zorn, N. F.; Asyuda, A.; Zharnikov, M.; Hogele, A.; Zaumseil, J. Synthetic Control over the Binding Configuration of Luminescent sp3-Defects in Single-Walled Carbon Nanotubes. *Nat. Commun.* **2021**, *12*, 2119.

(47) Gifford, B. J.; Sifain, A. E.; Htoon, H.; Doorn, S. K.; Kilina, S.; Tretiak, S. Correction Scheme for Comparison of Computed and Experimental Optical Transition Energies in Functionalized Single-Walled Carbon Nanotubes. *J. Phys. Chem. Lett.* **2018**, *9*, 2460−2468.

(48) Kilina, S.; Ramirez, J.; Tretiak, S. Brightening of the Lowest Exciton in Carbon Nanotubes Via Chemical Functionalization. *Nano Lett.* **2012**, *12*, 2306−2312.

(49) Wang, P.; Kim, M.; Peng, Z.; Sun, C. F.; Mok, J.; Lieberman, A.; Wang, Y. Superacid-Surfactant Exchange: Enabling Nondestructive Dispersion of Full-Length Carbon Nanotubes in Water. *ACS Nano* **2017**, *11*, 9231−9238.

(50) Fagan, J. A.; Haroz, E. H.; Ihly, R.; Gui, H.; Blackburn, J. L.; Simpson, J. R.; Lam, S.; Hight Walker, A. R.; Doorn, S. K.; Zheng, M. Isolation of > 1 nm Diameter Single-Wall Carbon Nanotube Species Using Aqueous Two-Phase Extraction. *ACS Nano* **2015**, *9*, 5377−5390.

(51) Frisch, M. J.; Trucks, G. W.; Schlegel, H. B.; Scuseria, G. E.; Robb, M. A.; Cheeseman, J. R.; Scalmani, G.; Barone, V.; Petersson, G. A.; Nakatsuji, H.; Li, X.; Caricato, M.; Marenich, A. V.; Bloino, J.; Janesko, B. G.; Gomperts, R.; Mennucci, B.; Hratchian, H. P.; Ortiz, J. V.; Izmaylov, A. F., et al. *Gaussian 09*; Gaussian, Inc.: Wallingford, CT, 2009.

(52) Yanai, T.; Tew, D. P.; Handy, N. C. A New Hybrid Exchange−Correlation Functional Using the Coulomb-Attenuating Method (CAM-B3LYP). *Chem. Phys. Lett.* **2004**, *393*, 51−57.

(53) Binkley, J. S.; Pople, J. A.; Hehre, W. J. Self-Consistent Molecular Orbital Methods. 21. Small Split-Valence Basis Sets for First-Row Elements. *J. Am. Chem. Soc.* **1980**, *102*, 939−947.

(54) Martin, R. L. Natural Transition Orbitals. *J. Chem. Phys.* **2003**, *118*, 4775−4777.

https://doi.org/10.1021/acsnano.1c07669
ACS Nano 2022, 16, 2077−2087